



Statistical analysis of spatter velocity with high-speed stereovision in laser powder bed fusion

Christopher Barrett¹ · Carolyn Carradero¹ · Evan Harris¹ · Kirk Rogers² · Eric MacDonald¹ · Brett Conner¹

Received: 13 December 2018 / Accepted: 24 July 2019 / Published online: 23 August 2019
© Springer Nature Switzerland AG 2019

Abstract

As unprecedented design freedom is realized through additive manufacturing and simultaneously as the diversity of materials improves to include high-performance metals, aerospace and biomedical applications demand improved quality control measures. In the context of additive manufacturing, new opportunities for in situ monitoring are now possible with a qualify-as-you-go layer-by-layer methodology. In this study, a pair of low-cost, high-speed cameras recording the selective laser melting of maraging steel was synchronized to measure stereoscopic features of the resulting spatter. Through epipolar geometry, accurate measurements were calculated of the age, speed and direction of thousands of spatter events. Statistical analysis was performed focusing on spatter velocity with the driving hypothesis that velocity can be correlated to the weld quality and eventually leveraged in real-time process control. Opportunities, future work, and challenges are discussed.

Keywords Direct metal laser sintering · Stereovision · Spatter · Velocity

1 Introduction

The aerospace industry has been exploring powder bed fusion (PBF) to create lightweight and complex structures fabricated with high-performance metal alloys. However, to broaden industrial adoption of PBF for flight critical structures, evidence of reliability will need to be collected layer by layer for each fabrication—particularly in light of the high standards in the aerospace industry and the general lack of flight heritage for additive manufacturing in general. The unobstructed view of the exposed top surface during the layerwise PBF fabrication allows for the monitoring in an unprecedented manner including both the melt pool and the associated ejecta. A qualify-as-you-go in situ methodology will be required to ensure the reliability.

Within the family of PBF processes, metal laser powder bed fusion (M-LPBF) has been optimized to fabricate complex structures with a diversity of metal powders. This process operates by focusing a laser onto a uniform layer of powder, which selectively melts (welds) the powder to a baseplate or previous layers of melted powder (Fig. 1). Process feedback is generally limited from most commercial grade systems and will be an inevitable requirement for the full qualification of AM-fabricated structures due to a general lack of confidence in the existing open-loop systems [1]. Metal ejecta (spatter) during the lasing process is a common occurrence and has been examined previously to determine or predict the quality of the melt and resulting fabricated structure [2–5]. The final destination of the spatter after ejection can fall within the boundaries of the structure under fabrication thereby introducing contamination of unintended material in subsequent layers. Building of high-quality structures today requires knowledge, careful observation and planning of part build order relative to laser location and gas flow in the powder bed system to minimize the effects of spatter. Furthermore, along the trajectory of the spatter, the material can occlude the laser, resulting in shadowing which may cause lack-of-fusion defects.

Electronic supplementary material The online version of this article (<https://doi.org/10.1007/s40964-019-00094-6>) contains supplementary material, which is available to authorized users.

✉ Christopher Barrett
cbarrett@student.yzu.edu

¹ Youngstown State University, Youngstown, OH 44555, USA

² Youngstown Business Incubator, Youngstown, OH 44503, USA

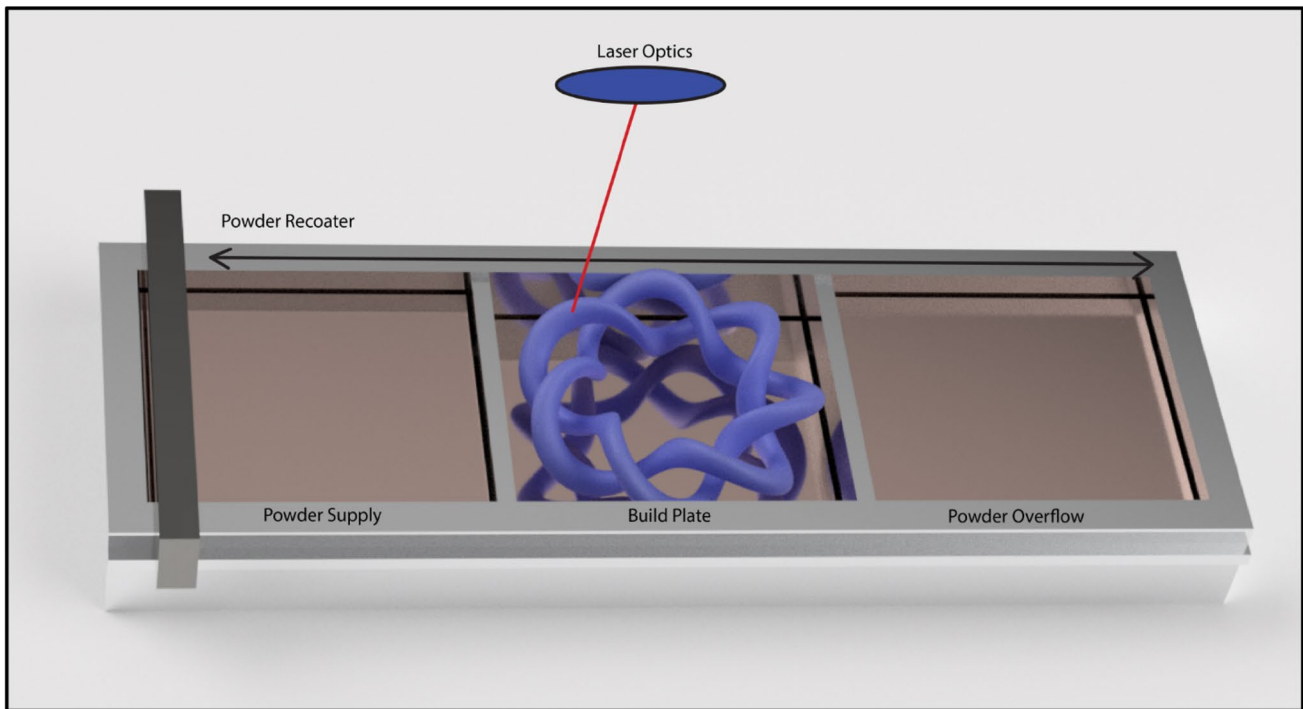


Fig. 1 Common LPBF layout

1.1 Previous work of others

Defects in M-LPBF include lack of fusion [6], spatter [7], keyholing [8], residual gas porosity [9], balling [10], hatching strategy defects and recoater defects [11]. Non-destructive evaluation and in situ monitoring was overviewed by [12] and demonstrates the necessity of further advance in these topics, specifically for eventual closed-loop control in LPBF. This article assumes that various laser parameters could lead to differing spatter velocities and therefore proposes an effective and financially feasible way to record these velocities in real time. These velocities not only provide valuable insight into physics-based models such as those proposed by Cunningham et al. [10], but also will improve intuition for determining the optimal noble gas recirculation flow (often available on commercial systems) across the powder bed to redirect spatter from contaminating the build. Spatter landing on the melting section has been reported to negatively impact the subsequent layers, as the ejecta are often larger in size than the average powder and layer sizes, and could contain oxidation contamination [7, 10, 13–16].

The ultimate goal of in situ monitoring is to provide feedback control. Behaviors of spatter in M-LPBF have been explored previously, but none have used high-speed stereovision at the macro level to observe overall trends in optimal build conditions [2, 5, 17–19]. [20–24]

investigated monitoring the process at the melt pool by measuring the melt pool shape and temperature, and although the origin of spatter is the melt pool, this is beyond the scope of the present work. The essence of M-LPBF is the melt pool, which is vital to understanding the quality of a fabrication; previous work has monitored and tracked the scan path which anecdotally has a significant impact on the amount and direction of spatter [25–29]. This work is intended to identify spatter behavior and thereby inform the process with the goal of eventually providing feedback for closed-loop control.

Utilizing high-speed digital videography to characterize spatter has been done in several studies. Frame rates have varied between 1000 frames per second (fps) and 6000 fps [5, 17, 30]. Thermal high-speed cameras have been used as well [7]. Ultra-high-speed imaging (100,000 fps or more) has led to breakthroughs in spatter-creating mechanisms, which may be the result of vapor-driven entrainment of micro-particles by an ambient gas flow [31]. This work detailed three types of particles using SS 316L and Ti64, the first have a low vertical momentum and are consumed by the melt pool, the second of which have higher vertical momentum but originated more than two melt pool widths away from the beam and were declared as “cold particles”, and the third, being the most common which are the incandescent hot particles and have a similar vertical momentum as the second type. The authors also concluded that 60% of spatter particles observed are the third category with approximate

velocities of 6–20 m/s, while the first and second categories had 3–8 m/s and 2–4 m/s, respectively.

Recently, Guo et al. and Zhao et al. have utilized high-speed X-ray imaging to monitor melt pool and spatter formation [32, 33]. The work shows great insights into the balance between the Marangoni flow and recoil pressure forces which can be combined to create spatter as well as keyhole defects. Spatter was noted on landing sights which lead to the creation of lack of fusion defects in the layer.

Previously, the authors had preliminarily laid the basis for this work without fully developing the algorithms to work on bulk data sets [13, 34]. This work focuses on showing that bulk statistical measurements of the spatter can be ascertained with minor financial investment and is feasible as a monitoring tool for build weld quality. It is believed that these results can further be used in the development and verification of physics-based models.

2 Methods and materials

The goal of this study is to statistically quantify the velocity of spatter under recommended conditions. An EOS M290 M-LPBF system was utilized with 18% Ni maraging 300 (MS1) steel powder with a laser power of 285 Watts, scanning speed of 960 mm/s, hatch spacing of 0.11 mm, and 40-micron layers. A low-cost system (defined here as less than \$10,000 USD) was developed to facilitate adoption and reproducibility. Calibration and camera mount design were crucial to gain accurate measurements from the system and are available from the authors.

2.1 High-speed stereovision camera system

Two low-cost, high-speed cameras (FPS 1000HD, The Slow Motion Camera Company, United Kingdom) were purchased, and a stiff mount was built using ULTEM™ 9085 to minimize any movement relative between the cameras, thereby allowing for standardization during calibration and live spatter measurements. Images were taken with 1280 × 720 pixels in raw format with an 18 mm lens. The camera system was mounted in front of an EOS M290 such that the images were captured through the front port window. The image field of view was 279 mm by 214 mm at the calculated 559 mm working distance, and the calculated pixel size was 0.064 mm². Figure 2 displays the M-LPBF system and a schematic of the camera system configuration.

2.2 Stereovision and epipolar geometry to identify velocity and direction of spatter

For calibration, intrinsic parameters were obtained which include information on the camera calibration matrix (K) and distortion coefficient as described in [34]. The former matrix is given by

$$K = \begin{bmatrix} f_x & 0 & c_x \\ 0 & f_y & c_y \\ 0 & 0 & 1 \end{bmatrix} \quad (1)$$

where K is camera calibration matrix, f_x and f_y are focal lengths in pixel units, and c_x and c_y are principal points, typically at the center of the image. The open source Computer Vision (OpenCV) library was used to locate features

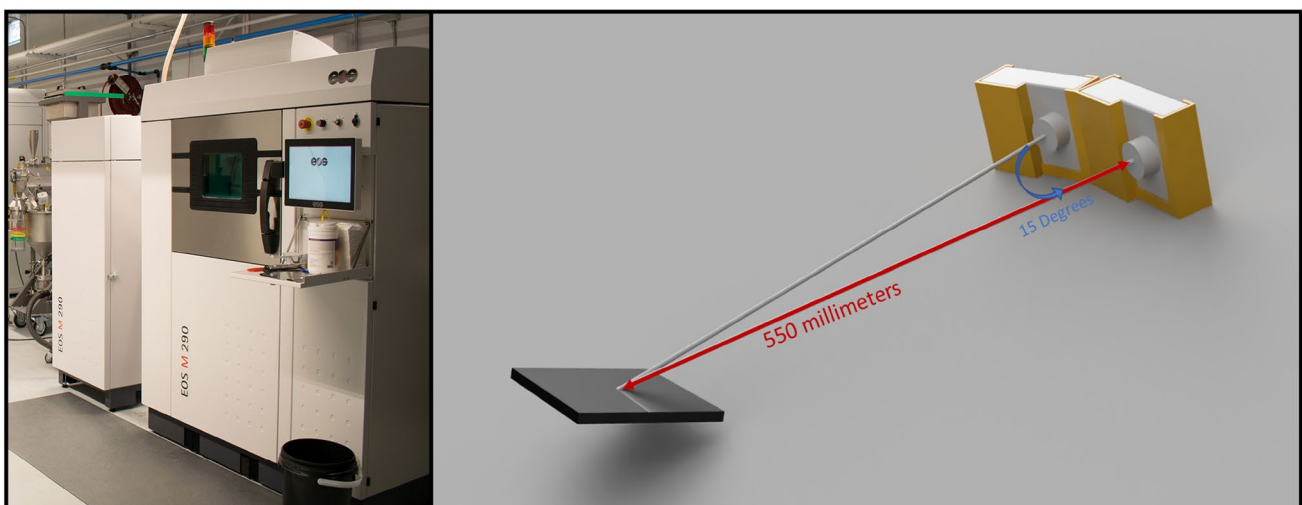


Fig. 2 EOS M290 with front port window (left) and stereovision schematic imaged through the window showing distance to build plate and corresponding angle (right)

on a checkerboard in manifold positions (Fig. 3). OpenCV is an open source computer vision library that is maintained by Intel, Inc. (Palo Alto, CA, USA). The intrinsic parameters are applied to provide stereo calibration, in which two images captured simultaneously provide the extrinsic parameters corresponding to the rotation (R) and translation (t) between the two cameras,

$$P = K[I|0] \quad (2)$$

$$P' = K'[R|t] \quad (3)$$

where P is a 3×4 projection matrix, I is the identity matrix, R is the rotation matrix and t is the translation matrix. The calibrated matrices are used to correct the two simultaneous frames using OpenCV with rectification to apply a correction transformation on both images. The projection matrices were then used to triangulate two matched points between the simultaneous frames. This method translates a pair of row and column values for the two matched points to a three-dimensional point within the build volume. By locating two points representing the beginning and end of a spatter, the speed, direction, and age can be calculated.

To validate the technique in a simulated measurement, two images of a caliper were captured (Fig. 4). By identifying two points, the distance between both was measured. The distance of the first measurement between the two points in the caliper was 50.01 mm, while the distance measured with stereovision was 50.690 mm, producing an error of 1.34%. The second distance was 9.99 mm, while the distance measured with stereovision was 9.986 mm, producing an error of 0.04% (which is less precise as it is below the accuracy of the caliper).

2.3 Computer vision algorithm

A computer vision algorithm was utilized to identify spatter and find average vector lengths. As the exposure time for each frame was 500 μ S, incandescent spatter was smeared

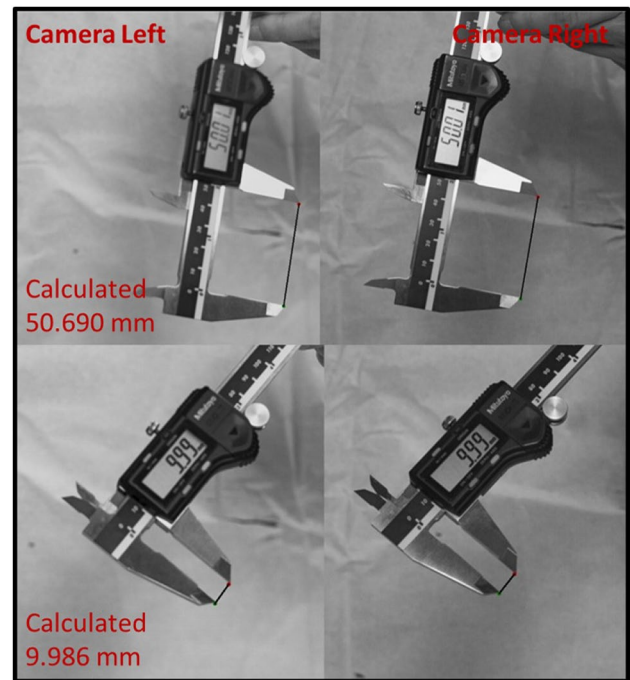
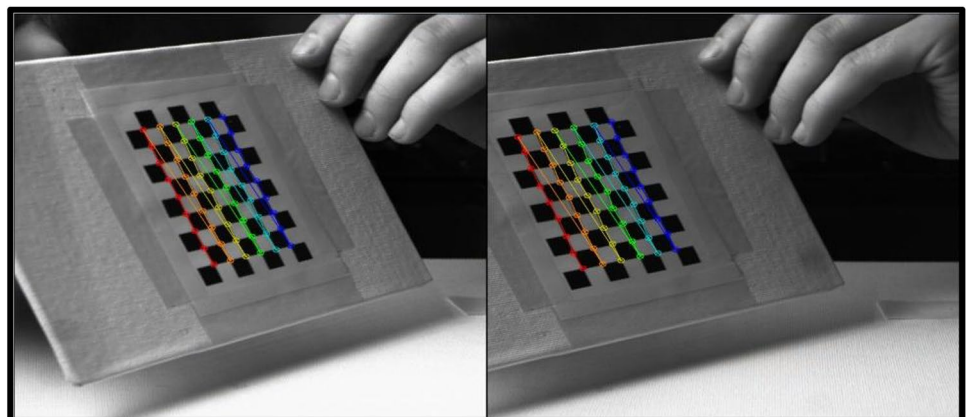


Fig. 4 Stereovision quality assurance using a caliper (50.01 mm top, 9.99 mm bottom). Red text represents the 3D coordinates for the first point, the green for the second and the blue represents the 3D distance between both. OpenCV was used to measure the values and print the text on the pictures

across the image due to overexposure—a flaw that was leveraged to calculate the average velocity. Using stereovision, the start and stop of each overexposed line were calculated in three-dimensional space. The algorithm for identifying the spatter line on two simultaneous images included converting the images to grayscale and then thresholding to locate all bright features. As spatter became progressively darker with age, the brightness was used to filter the spatter to identify each spatter only once—although most spatter can be seen on multiple sequential frames. Additional filtering

Fig. 3 Stereo calibration between images coincidentally captured by two cameras



was implemented by identifying the general location of the melt pool within an image and then locating all high-aspect ratio contours (length five times greater than width). If the estimated line of the long contour projected back through the melt pool, the location of the spatter start and stop pixels were recorded and all other contours were ignored. By identifying the start and stops of any single spatter from two perspectives, the 3D length could be calculated with epipolar geometry. Given the length was traversed over a 500 μs exposure time, the velocity can be calculated—the main objective of this effort. One challenge with this method is that the glow of the spatter inherently makes the spatter appear larger, which leads to a basic error in the measurements—particularly for shorter (slower) spatter. Future efforts will optimize exposure times to reduce this error and will also consider methods for estimating the particle size based on the width of the contour—assuming the particles generally have an aspect ratio of one and are spherical.

3 Results and discussion

A build of maraging steel was performed on an EOS M290, and a 7-s video was taken at 1000 frames per second to determine bulk spatter statistics resulting in 7000 images. The cameras were mounted outside of the chamber window and utilized 18 mm lenses.

3.1 Velocity subset validation of stereovision tracking

To gain insight and validate the algorithm, a subset of images was taken with the laser turning a corner and starting in the opposite direction with the hatch. Three subsequent images were taken after the turn to track the spatter and gain triplicate measurements and spatter were typically able to be tracked for three subsequent images before they faded and became too difficult to track. Although not all spatter were detected in the three images, 50 spatter were identified and direction was calculated (Fig. 5). Spatter just after a change in laser hatching direction were chosen, because it presented a clean set of data without the laser creating flash points when it ignited soot directly over the melt pool (false positive detections) and allowed for a manual check of the data to ensure all the spatter were appropriately detected to avoid false negative detections. This spatter was then analyzed via the developed algorithm and the start and end points of the spatter streak verified manual to determine the average population velocity and magnitude of the corresponding vectors and is shown in Table 1. This resulted in an average velocity of 9.38 m/s, with a minimum detection of 2.98 m/s and a maximum of 27.60 m/s which is consistent with the analysis of Ly et al. [31] which listed their approximated range

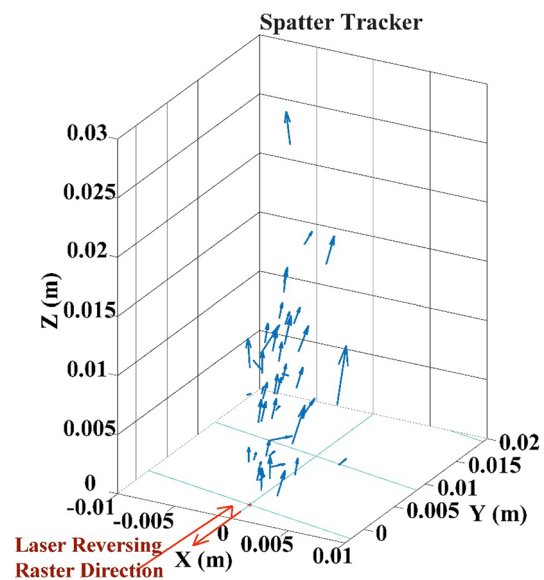


Fig. 5 Spatter detected on edge of part as laser path is changing direction, laser direction indicated showing path during spatter formation

as 2–20 m/s. This clean and verified dataset average would then be used to compare to the full set of images to ensure similarity in results.

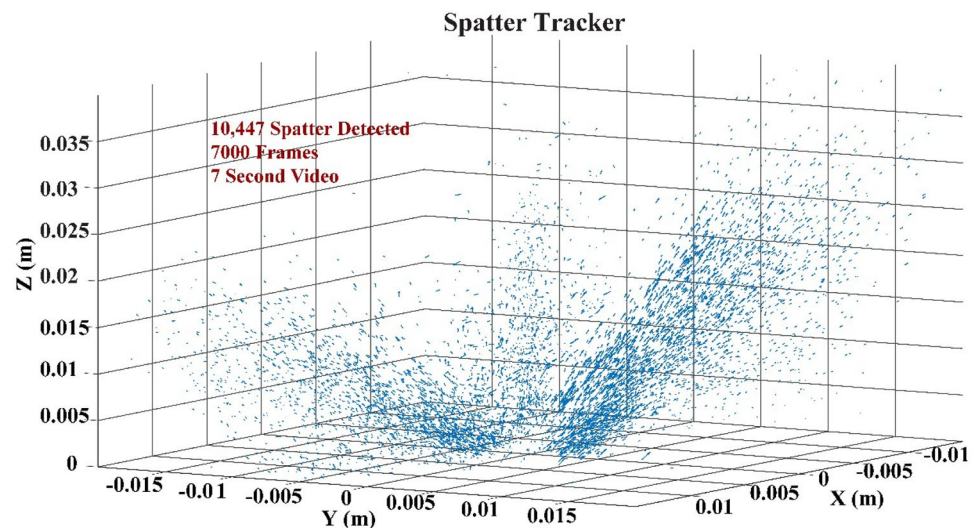
3.2 Stereo imaging of spatter and determination of bulk statistical velocity

The algorithm was then allowed to run over the entire 7 s of video which at 1000 fps generated 7000 paired images. Autodetection of spatter was utilized and the magnitude and velocity of the spatter were found. The results are plotted in Fig. 6 with their vectors in three-dimensional space, relative to the centroid of the melt pool of the previous frame and this was set to the origin to allow for the visualization of the spatter's detected location in regard to the melt pool. 10,447 spatter were detected over the 7-s video, which includes duplicate and triplicate detections as at 1000 fps most spatter could clearly be seen multiple times. It is believed that these multiple detections could be of benefit when working with the average velocity as they would increase the weight of valid detections. However, this will statistically make the average velocity slower as the faster particles are detected fewer times and so therefore have less weight on the overall average. Of note, false positives can be seen primarily in the central region directly above the melt pool. These are assumed to be soot that was irradiated by the laser and not spatter, this was verified by a manual check of various images where the results occurred and it was found that the particles were often directed down instead of up from a clear origin from

Table 1 Spatter detected on edge of part with laser turning to head in opposite direction, first ten results shown with bulk statistics below, exposure of 500 μ s

Particle #	Start ([x, y, z], mm)	End ([x, y, z], mm)	Magnitude (mm)	Velocity (m/s)
1	[−1.496, 4.867, 6.798]	[−1.553, 7.087, 10.83]	3.97	7.93
2	[−1.463, 7.379, 8.989]	[−1.877, 9.662, 12.96]	4.60	9.19
3	[−2.822, 10.69, 14.07]	[−2.903, 12.64, 17.27]	3.76	7.51
4	[−0.8661, 2.997, 1.628]	[−1.175, 4.841, 2.921]	2.27	4.55
5	[−0.5894, 4.635, 5.372]	[−0.724, 7.155, 9.521]	4.86	9.71
6	[−0.4848, 4.122, 0.4827]	[−2.188, 7.403, 4.562]	5.51	11.01
7	[−0.3990, 1.863, 1.249]	[−0.6433, 3.815, 3.573]	3.04	6.09
8	[0.2354, 2.790, 4.426]	[4.839, 5.104, 5.590]	5.28	10.56
9	[−1.895, 5.238, 10.37]	[0.6655, 9.580, 16.50]	7.94	15.88
10	[−0.8180, 4.122, 2.336]	[−1.135, 6.360, 5.510]	3.90	7.79
Avg. velocity population ($n=50$)				9.38
St. dev. p population ($n=50$)				4.42
Maximum				27.60
Minimum				2.98

Fig. 6 10,447 spatter magnitude vectors plotted centering each spatter to the same origin point, detected over a 7-s imaging period

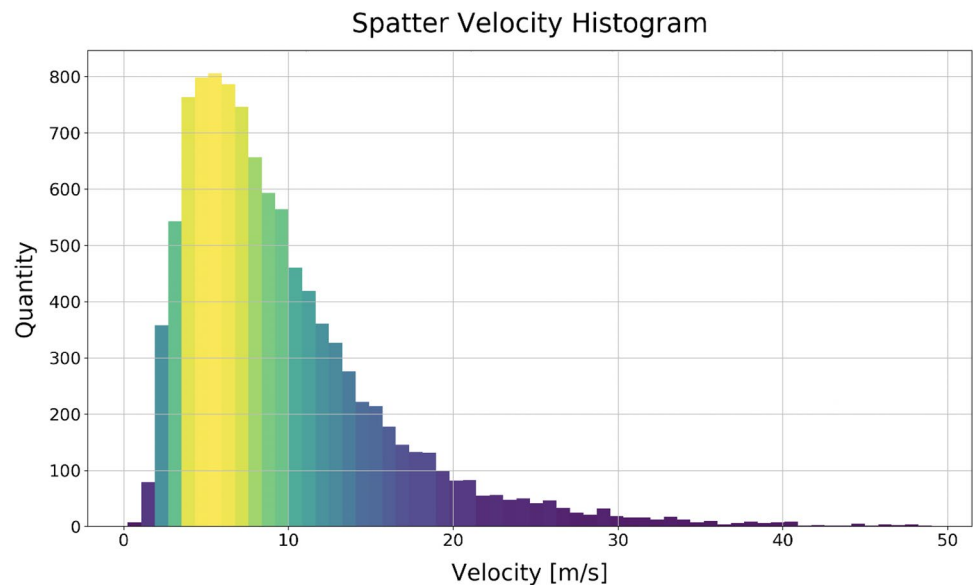


the melt pool. Further work is currently underway to automatically ignore these detection results. Table 2 shows the statistical results of the analysis with the first ten detections similarly to Table 1. The average velocity over the entire set was 9.73 m/s which had good agreement with the previous subset of data having only a 0.35 m/s or 3.66% difference. The maximum value detected, and the minimum value showed a dramatically increased range. The current algorithm does not allow for sorting of detected spatter and determination of which images correspond to which detection, so we are currently unable to examine the maximum and minimum values to determine their validity. This feature is currently being added and is expected to aid in the removal of false positives or negatives. Figure 7 shows the histogram of the bulk results with the majority of the spatter being detected between 1.5 and 14.5 m/s.

Future work is currently being performed to more accurately sort out false positive or negatives; however, it is believed that the average velocity of the group and bulk statistical results will not change substantially. Additionally, the algorithm is being modified to allow for the determination of which spatter has been detected multiple times so that appropriate weighting of the average can occur. Further analysis is also under way to compare the bulk spatter data under various laser parameters sets below and above recommended values, multiple printing platforms, and material types. The average velocity for these groups is posited to shift accordingly with the intention being that various platforms will have similar results with similar processing parameters and material types. Further work is also being performed to track the average direction based on the origin in the melt pool with respect to the melt pool centroid.

Table 2 Measured beginning and end points for first ten spatters from Fig. 6, their calculated magnitudes and velocities, and bulk statistical results

Particle #	Start ([x, y, z], mm)	End ([x, y, z], mm)	Magnitude (mm)	Velocity (m/s)
1	[−1.496, 4.867, 6.798]	[−1.553, 7.087, 10.83]	1.61	3.23
2	[−1.463, 7.379, 8.989]	[−1.877, 9.662, 12.96]	4.18	8.35
3	[−2.822, 10.69, 14.07]	[−2.903, 12.64, 17.27]	2.28	4.55
4	[−0.8661, 2.997, 1.628]	[−1.175, 4.841, 2.921]	2.14	4.29
5	[−0.5894, 4.635, 5.372]	[−0.724, 7.155, 9.521]	10.13	20.25
6	[−0.4848, 4.122, 0.4827]	[−2.188, 7.403, 4.562]	2.11	4.21
7	[−0.3990, 1.863, 1.249]	[−0.6433, 3.815, 3.573]	1.30	2.60
8	[0.2354, 2.790, 4.426]	[4.839, 5.104, 5.590]	1.48	2.97
9	[−1.895, 5.238, 10.37]	[0.6655, 9.580, 16.50]	4.76	9.53
10	[−0.8180, 4.122, 2.336]	[−1.135, 6.360, 5.510]	1.84	3.68
Avg. velocity population ($n = 10,447$)				9.73
St. dev. p population ($n = 10,447$)				6.74
Maximum				79.64
Minimum				0.26

Fig. 7 10,447 spatter detected graphed with velocity versus frequency

4 Conclusion

In conclusion, a low-cost spatter tracking method and analysis for laser powder bed fusion has been presented along with initial statistical results. The system can be used to collect real-time statistical data on the spatter behavior of a process and may have utility in terms of measuring the performance of the process. This paper demonstrates the tenets of the proposed in situ measurement system and the key completed objectives of this work are as follows:

- Reliable collection of the demonstrated statistics relating to spatter velocities gathered by stereovision over 1000 s of frames.
- An open source and low-cost (less than \$10,000 USD) hardware and software system was successfully implemented.

- Initial results of collected statistical data are reported which demonstrate that the data are in line with previous reports but now can be captured in a continuous and real-time data collection system.
- Utilizing the stereovision setup enabled increased accuracy in the measurement for velocity and quantity.

Acknowledgements We would like to thank the Friedman Endowment for Manufacturing at Youngstown State University. This effort was performed in part through the National Center for Defense Manufacturing and Machining under the America Makes Program entitled “Maturation of Advanced Manufacturing for Low Cost Sustainment (MAMLS)” and is based on research sponsored by Air Force Research Laboratory under agreement number FA8650-16-2-5700. The U.S. Government is authorized to reproduce and distribute reprints for Governmental purposes notwithstanding any copyright notation thereon.

References

- Berumen S, Bechmann F, Lindner S, Kruth J-P, Craeghs T (2010) Quality control of laser- and powder bed-based additive manufacturing (AM) technologies. *Phys Procedia* 5:617–622
- Liu Y, Yang Y, Mai S, Wang D, Song C (2015) Investigation into spatter behavior during selective laser melting of AISI 316L stainless steel powder. *Mater Des* 87:797–806
- Gunenthiram V, Peyre P, Schneider M, Dal M, Coste F, Koutiri I, Fabbro R (2018) Experimental analysis of spatter generation and melt-pool behavior during the powder bed laser beam melting process. *J Mater Process Technol* 251:376–386
- Bidare P, Bitharas I, Ward RM, Attallah MM, Moore AJ (2018) Fluid and particle dynamics in laser powder bed fusion. *Acta Mater* 142:107–120
- Repossini G, Laguzza V, Grasso M, Colosimo BM (2017) On the use of spatter signature for in situ monitoring of laser powder bed fusion. *Addit Manuf* 16:35–48
- Tang M, Pistorius PC, Beuth JL (2017) Prediction of lack-of-fusion porosity for powder bed fusion. *Addit Manuf* 14:39–48
- Criales LE, Arsoy YM, Lane B, Moylan S, Donmez A, Özel T (2017) Laser powder bed fusion of nickel alloy 625: experimental investigations of effects of process parameters on melt pool size and shape with spatter analysis. *Int J Mach Tools Manuf* 121:22–36
- King WE, Barth HD, Castillo VM, Gallegos GF, Gibbs JW, Hahn DE, Kamath C, Rubenchik AM (2014) Observation of keyhole-mode laser melting in laser powder-bed fusion additive manufacturing. *J Mater Process Technol* 214:2915–2925
- Cunningham R, Narra SP, Montgomery C, Beuth J, Rollett AD (2017) Synchrotron-based X-ray microtomography characterization of the effect of processing variables on porosity formation in laser powder-bed additive manufacturing of Ti–6Al–4 V. *JOM* 69:479–484
- Khairallah SA, Anderson AT, Rubenchik A, King WE (2016) Laser powder-bed fusion additive manufacturing: physics of complex melt flow and formation mechanisms of pores, spatter, and denudation zones. *Acta Mater* 108:36–45
- Foster BK, Reutzel EW, Nassar AR, Hall BT, Brown SW, Dickman CJ (2015) Optical, layerwise monitoring of powder bed fusion. In: *Proceedings of solid freeform fabrication symposium*. pp 295–307. sffsymposium.engr.utexas.edu
- Everton SK, Hirsch M, Stravroulakis P, Leach RK, Clare AT (2016) Review of in situ process monitoring and in situ metrology for metal additive manufacturing. *Mater Des* 95:431–445
- Barrett C, Walker J, Enriquez Gutierrez R, MacDonald E, Conner B (2018) A low cost, high-speed optical monitoring system for tracking spatter during laser powder bed fusion. In: *TMS 2018*. Phoenix
- Kneen TJ (2016) Characterizing the high strain rate mechanical behavior of stainless steel 316L processed by selective laser melting. Youngstown State University
- Mumtaz K, Hopkinson N (2009) Top surface and side roughness of Inconel 625 parts processed using selective laser melting. *Rapid Prototyp J* 15:96–103
- Ladewig A, Schlick G, Fisser M, Schulze V, Glatzel U (2016) Influence of the shielding gas flow on the removal of process by-products in the selective laser melting process. *Addit Manuf* 10:1–9
- Taheri Andani M, Dehghani R, Karamooz-Ravari MR, Mirzaeifar R, Ni J (2018) A study on the effect of energy input on spatter particles creation during selective laser melting process. *Addit Manuf* 20:33–43
- Taheri Andani M, Dehghani R, Karamooz-Ravari MR, Mirzaeifar R, Ni J (2017) Spatter formation in selective laser melting process using multi-laser technology. *Mater Des* 131:460–469
- Simonelli M, Tuck C, Aboulkhair NT, Maskery I, Ashcroft I, Wildman RD, Hague R (2015) A study on the laser spatter and the oxidation reactions during selective laser melting of 316L stainless steel, Al–Si10–Mg, and Ti–6Al–4V. *Metall Mater Trans A* 46:3842–3851
- Craeghs T, Bechmann F, Berumen S, Kruth J-P (2010) Feedback control of layerwise laser melting using optical sensors. *Phys Procedia* 5(Part B):505–514
- Clijsters S, Craeghs T, Buls S, Kempen K, Kruth J-P (2014) In situ quality control of the selective laser melting process using a high-speed, real-time melt pool monitoring system. *Int J Adv Manuf Technol* 75:1089–1101
- Lott P, Schleifenbaum H, Meiners W, Wissenbach K, Hinke C, Bültmann J (2011) Design of an optical system for the in situ process monitoring of selective laser melting (SLM). *Phys Procedia* 12(Part A):683–690
- Yadroitsev I, Krakhmalev P, Yadroitsava I (2014) Selective laser melting of Ti6Al4V alloy for biomedical applications: temperature monitoring and microstructural evolution. *J Alloys Compd* 583:404–409
- Doubenskaia M, Pavlov M, Grigoriev S, Tikhonova E, Smurov I (2012) Comprehensive optical monitoring of selective laser melting. *J Laser Micro Nanoeng* 7:236–243
- Kanko JA, Sibley AP, Fraser JM (2016/5) In situ morphology-based defect detection of selective laser melting through inline coherent imaging. *J Mater Process Technol*. 231: 488–500
- Krauss H, Eschey C, Zaeh M (2012) Thermography for monitoring the selective laser melting process. In: *Proceedings of the solid freeform fabrication symposium*
- Lane B, Moylan S, Whitenton E, Ma L (2016) Thermographic measurements of the commercial laser powder bed fusion process at NIST. *Rapid Prototyp J* 22:778–787
- Bayle F, Doubenskaia M (2008) Selective laser melting process monitoring with high speed infra-red camera and pyrometer. In: *Fundamentals of laser assisted micro- and nanotechnologies*. International Society for Optics and Photonics, pp 698505–698508
- Grasso M, Laguzza V, Semeraro Q, Colosimo BM (2017) In-process monitoring of selective laser melting: spatial detection of defects via image data analysis. *J Manuf Sci Eng* 139:051001
- You D, Gao X, Katayama S (2014) Monitoring of high-power laser welding using high-speed photographing and image processing. *Mech Syst Signal Process* 49:39–52
- Ly S, Rubenchik AM, Khairallah SA, Guss G, Matthews MJ (2017) Metal vapor micro-jet controls material redistribution in laser powder bed fusion additive manufacturing. *Sci Rep* 7:4085
- Guo Q, Zhao C, Escano LI, Young Z, Xiong L, Fezzaa K, Everhart W, Brown B, Sun T, Chen L (2018) Transient dynamics of powder spattering in laser powder bed fusion additive manufacturing process revealed by in situ high-speed high-energy X-ray imaging. *Acta Mater* 151:169–180
- Zhao C, Fezzaa K, Cunningham RW, Wen H, De Carlo F, Chen L, Rollett AD, Sun T (2017) Real-time monitoring of laser powder bed fusion process using high-speed X-ray imaging and diffraction. *Sci Rep* 7:3602
- Barrett C, Carradero-Santiago C, Harris E, Mc Knight J, Walker J, MacDonald E, Conner B (2018) Low cost, high speed stereovision for spatter tracking in laser powder bed fusion. In: *Solid freeform fabrication symposium*

Publisher's Note Springer Nature remains neutral with regard to jurisdictional claims in published maps and institutional affiliations.